

Detection of guided waves between gas wells for reservoir characterization

Jorge O. Parra*, Chris L. Hackert*, Anthony W. Gorody[‡],
and Valeri Korneev**

ABSTRACT

Guided seismic waves can be used to predict continuity and discontinuity of reservoir structures between wells, with the low-velocity beds acting as waveguides. We relate guided-wave signatures to waveguide targets using experimental data acquired at the Stratton gas field in southeast Texas. The observed seismic data indicate the presence of trapped energy in low velocity shale markers between wells 145 and 151. Guided waves in the form of leaky modes are excited, transmitted, and detected in the low-velocity shale markers at a well separation of 1730 ft (527 m). Dispersion analysis, modeling, frequency–amplitude depth curves, well logs, and lithological information all support the results. Specifically, the characterization of two low-velocity shale markers, V2 and V5, demonstrates that V2 is more heterogeneous than V5 between the source well 151 and detector well 145. Finally, images of synthetic and real data show the potential applications of the guided-wave technology as a tool for reservoir characterization.

INTRODUCTION

An interwell seismic technique that can predict continuity and discontinuity of geological targets between wells would be a powerful tool for characterizing hydrocarbon reservoirs. However, to apply such a technique properly we should be able to demonstrate experimentally that guided waves can be excited, transmitted, and detected between gas wells. Also, we should be able to identify the presence of such events in the interwell seismic data. For planning purposes, Parra et al. (1998) demonstrate, using computer models based on realistic petrophysical parameters, that guided waves can be transmitted and detected at distances >800 m. They also demonstrate experimentally that guided waves can be detected at a well separation of 100 m at the Gypsy test site, Oklahoma. Recently, field experiments completed at the Stratton gas field, Nueces county, Texas, confirm that low-velocity shale layers can trap seismic energy between wells at distances >800 m. The geologic characteristics of the low-velocity shales at the Stratton field and practical applications for continuity logging are discussed in Gorody and Parra (1999). Although continuity logging (or in-seam seismic) is a method commonly used in coal geophysics to determine structures such as clay dikes and faults in coal seams (Buchanan, 1993), this method has not been truly demonstrated in hydrocarbon fields.

We show for the first time that guided waves can be excited, transmitted, and detected between gas wells in the upper Frio Formation, southeast Texas. We attempt to answer two questions about the applicability of guided waves for reservoir characterization:

- 1) Can we experimentally excite, transmit, and detect guided waves at well separations comparable to those encountered between gas wells?
- 2) Can we identify the presence of guided waves in real interwell seismic data?

Interwell seismic data recorded at the Stratton gas field, data processing, and computer model responses provide an affirmative answer to our questions. We evaluate the presence of guided waves in the observed data using signal analysis and computer models based on real petrophysical parameters. In the current evaluation of the guided-wave technology, we did not have the resources to conduct a second experiment in the middle and lower Frio Formations, where the geology is discontinuous. However, we address this issue by introducing images of synthetic data to show how discontinuous and continuous targets can be identified from synthetic seismic data. Since the real data were acquired in the more continuous upper Frio Formation, we present a real image only for a geological shale marker.

Manuscript received by the Editor August 30, 1999; revised manuscript received April 16, 2001.

*Southwest Research Institute, P.O. Drawer 28510, San Antonio, Texas 78238-0510. E-mail: jparra@swri.edu; chackert@swri.edu.

[‡]Universal Geoscience Consulting, Inc., 11807 Taylorcrest Rd., Suite One, Houston, Texas 77024. E-mail: agorody@compuserve.com.

**Lawrence Berkeley National Laboratory. E-mail: vakorneev@lbb.gov.

© 2002 Society of Exploration Geophysicists. All rights reserved.

METHOD OF COMPUTATION AND ANALYSIS

Continuity logging method

The continuity logging method consists of placing a seismic source in one borehole in a low-velocity zone and deploying a detector array in a second borehole. Detection of dispersive waves excited by the source in the waveguide and transmitted between wells, depending on the amplitude and dispersion characteristics of the response, can be an indicator of continuity in low-velocity zones.

The guided waves are leaky modes, normal modes, or both, excited in waveguides by critical refraction of seismic waves at the boundaries. Guided seismic waves are waves that experience geometric dispersion as a result of constructive interference within the waveguide. The leaky modes represent a constructive interference that mimics a type of normal mode where the P -wave energy is responsible for the constructive interference, while the S -wave energy is radiated from the waveguide. Normal modes consist of interacting P -wave and SV -particle motions that are trapped and propagated along the guiding layer as guided waves.

For a typical waveguide (low velocity) in a host medium (higher velocity), the seismic traces are dominated by head waves and leaky modes, which arrive after the head wave and before the direct P -wave. Head waves are refracted waves that propagate with the average P -wave velocity of the medium surrounding the waveguide (see Aki and Richards, 1980). A model study including sandstone and shale waveguides to evaluate the transmission and detection of guided waves in reservoir rock is given in Parra et al. (1998). Our model-based processing approach is presented to analyze full waveforms containing guided waves.

The properties of a propagating wave train (or a guided wave) can be described by its spectral representation at different locations in the waveguide. If we assume 1-D space, a wave package with displacement amplitudes $f(x, t)$ and the Fourier spectrum $f_o(\omega)$ at the source position $x_0 = 0$ which travels in the direction of the x -axis will change its shape according to (see Dresen and Ruter, 1994)

$$f(x, t) = \frac{1}{2\pi} \int_{-\infty}^{\infty} f_o(\omega) \exp[ik(\omega)x - \omega t] d\omega. \quad (1)$$

In a waveguide, $k(\omega) = k_n(\omega)$ is a nonlinear function, which depends on the physical properties of the medium and the boundary conditions of the model under consideration. The index n indicates a special branch (mode) of the phase velocity curve. The significant contributions to the integral are related to those frequencies where the phase $[k(\omega)x - \omega t]$ is stationary, which gives the relation

$$\frac{x}{t} = \left[\frac{d\omega}{dk} \right]_{\omega=\omega_0} = U(\omega_0). \quad (2)$$

For a particular frequency value ω_0 there are a number of space-time locations (x, t) on the straight line defined by $x/t = U(\omega_0)$, where ω_0 is the predominately contributing frequency to the amplitude of the wave train. This shows that the group velocity defined as $U(\omega) = d\omega/dk$ is the velocity of the wave group with a certain dominant frequency. To further explore the properties of the wave trains, we use an asymptotic representation of equation (1):

$$f(x, t) \cong \left[\frac{f_o(\omega_0)}{\sqrt{2\pi x k_0}} \right] \exp \left[i(k_0 x - \omega_0 t \pm \frac{\pi}{4}) \right], \quad (3)$$

where k_0 = the slope of the group velocity curve near ω_0 , which is obtained from the phase velocity of the waveguide mode. Equation (3) shows that at a large distance from the source, the original pulse is transformed into a train of sinusoidal waves in which frequency and amplitude vary gradually along the wave train. In addition the amplitude decreases with distance as $x^{-1/2}$ and is proportional to the spectral amplitude of the source at the dominant frequency. It also varies inversely proportional to the square root of the slope of the group velocity curve, k_0 . This suggests that steep parts of the group velocity curve are related to low amplitudes while flat sections of the curve give rise to high amplitudes of the wave train.

The above analysis is restricted to a wave formed by a dispersive signal composed of one single mode only. Contributions to the particle motion from other modes can be obtained in the same way. All of these contributions together form the complete dispersed wave train propagating in a waveguide.

Several methods have been developed to compute the phase velocity dispersion curves of layered structures (Dunkin, 1965; Kennett and Kerry, 1979; Rader et al., 1985; Laster et al., 1965; Dresen and Ruter, 1994). Expressions for the velocity equations are transcendental relationships that must be solved numerically in root-finding analysis for a simple three-layer case. By specifying the physical parameter of the various layers of rock, the mode number, and successive frequencies, the corresponding normal-mode phase velocity for each frequency can be derived. The recursive phase velocity algorithm of Rader et al. (1985) is an effective technique applicable to normal modes excited in a stratified medium of arbitrary, homogeneous, parallel isotropic layers.

An approach to simulate guided waves in a multilayered medium consists of establishing the wavefield solution based on the global matrix formulation (Schmidt and Tango, 1986; Mal, 1988; and Parra and Xu, 1994). In this approach the boundary conditions are satisfied in the form of the difference of field quantities across each layer interface. Thus, the general solution is obtained as a linear system of equations given by

$$\mathbf{G}\boldsymbol{\eta} = \mathbf{B}, \quad (4)$$

where \mathbf{G} is the global matrix composed of submatrices which contain coefficients associated with the physical properties of the rock bulk matrix and the coordinates of the interfaces. The vector \mathbf{B} contains the external excitations, and $\boldsymbol{\eta}$ represents the unknown wave coefficients, which are used to determine the wavefield. The elements of the submatrices of matrix \mathbf{G} and those of the vectors $\boldsymbol{\eta}$ and \mathbf{B} are addressed in the Appendix. The phase velocity of leaky and normal modes at a specified frequency are obtained by setting the determinant of the global matrix equal to zero, which represents a free excitation state:

$$\text{Det}[\mathbf{G}(k, \omega)] = 0. \quad (5)$$

A pole of this periodic equation corresponds to a complex wavenumber root $k = \text{Re}(k) + i \text{Im}(k)$ at a given frequency ω . The phase velocity of the mode is equal to $\omega/\text{Re}(k)$, while its attenuation Q^{-1} is equal to $2 \text{Im}(k)/\text{Re}(k)$. To search for the k values on the complex wavenumber plane that satisfies

equation (5), we use a 2-D bracketing and minimization technique given by Parra and Xu (1994).

To simulate the wave train, the general wave displacement solution for a point source in a layered-earth medium that is formed by several terms containing wavenumber integrals is considered (see Parra et al., 1993). The integrand of any of these displacement integrals (e.g., I_m) is a product of the kernel $T(k, z, \omega)$ and a Bessel function of the first kind, order n , i.e.,

$$I_m = \int T(k, z, \omega) J_n(kr) dk, \quad \text{for } n = 0, 1, 2, \quad (6)$$

where z and r are the vertical and horizontal distances between the source and the detector. The kernel function $T(k, z, \omega)$ is defined in Parra et al. (1993), and it contains complex poles which are slightly off the real axis toward the positive direction of the imaginary axis associated with the physical property of the medium. The complete motion can be separated into two main integrals. The first integral represents the body-wave part of the solution, and the second integral represents the guided-wave part. This second integral is evaluated analytically through contour integration and results in a sum of the residues (Kundu and Mal, 1985). Thus, the guided-wave part of the total displacement I_g is given by

$$I_g = \sum_{m=1}^M F[\text{Re}(p_m)] H_m^{(1)}(p_m r), \quad (7)$$

where $H_m^{(1)}$ denotes a Hankel function, p_m denotes a complex pole, M denotes the total number of poles, and F denotes the products of reflection and transmission matrices containing the physical properties of the layered medium. Thus, once the phase velocities of normal modes and leaky modes are obtained from equation (5), the guided-wave part of the wavefield for various source–detector locations can be calculated.

Computation and analysis

To determine whether guided waves are excited in a low-velocity zone in the Frio Formation at the Stratton gas field, we used the model-based processing approach for planning and processing continuity logging data. This approach requires lithological information, P - and S -wave velocity logs, and the density log. The input parameters are used to calculate dispersion and attenuation curves for the selected layered-earth structure. These curves give all the possible leaky and normal modes that can be excited by any given seismic source. Since well separations are known in the site, we calculate synthetic spectral responses based on the geological model and the rock physical property information derived from well logs. The spectral response helps select the source frequency excitation to produce synthetic seismograms at a given well separation at several source and detector positions. The next step is to compare the synthetic seismogram with observed seismograms.

In complicated geology as that at Stratton, we do not expect to match the observed and synthetic seismograms. For example, when leaky modes are observed in the waveforms, we use simple layer models to analyze them. The leaky modes can be recognized because their group velocity starts at the average P -wave velocity of the medium surrounding the waveguide and then decreases with increasing frequency to reach a group

velocity minimum. Then the velocity increases slowly toward the average P -wave velocity of the waveguide.

The group velocity curves can be obtained for a given layered model using equation (5). A practical comparison between the observed data and the calculated group velocity curves requires that we convert the observed waveforms into group velocity images (Cohen, 1989). Thus, to determine the dispersion characteristic of the leaky modes, we superimpose the theoretical dispersion curves calculated using equation (5) on the velocity images.

A different approach to identify guided waves is to plot amplitude–depth distribution curves directly from the continuity logging data. The magnitude of the wavefield along the line of detectors perpendicular to the layered medium is calculated for model parameters at several frequency values. These plots provide information on the symmetrical and asymmetrical characteristics of the mode excited by the source in the waveguide. These plots are easily compared with the lithology to locate waveguide boundaries (Dresen and Ruter, 1994; Parra, 1996). In this paper observed amplitude–depth distribution curves based on continuity logging data (recorded between gas wells) are compared with the corresponding synthetic curves to support the interpretation.

DATA ANALYSIS FOR PROOF OF CONCEPT

Background information

To demonstrate experimentally the transmission and detection of guided waves, we selected geological markers based on seismic reflectors and well logs from the upper Frio Formation at the Stratton gas field. Stratton is among the fields comprising the largest Texas gas play, the Frio FR-4 (Kosters et al., 1989). It was selected because it is one of the most extensively studied and well-documented producing oil and gas fields in the Gulf Coast (Levey et al., 1994). Since the Stratton field consists mainly of sandstones and shales of the Frio Formation (with velocity contrasts on the order of 10% to 20%), the selection of layered intervals for proof of concept was made using seismic lines derived from 3-D surveys. The analysis and interpretation of the seismic lines are given in Gorody and Parra (1999).

The most obvious features of the upper Frio Formation visible on seismic lines are the nearly horizontal, continuous, high-amplitude reflectors associated with two sand beds named A22 and A8, shown in Figure 1. The strong impedance contrasts between shales and sands in the formation impart a strongly layered appearance on seismic lines. The optimum low-velocity zones were selected on the basis of these strong, laterally continuous impedance contacts. Analysis of sonic logs reveals a direct correlation between lows on the resistivity logs and low-velocity zones among the fieldwide markers. Thus, the strong seismic impedance contrast results from the juxtaposition of low-velocity shale layers and higher velocity sands.

Three low-velocity intervals were identified, from top to bottom, as the V2, V5, and V12 shale zones. These low-velocity zones are recognizable in all the wells illustrated in Figure 1. The relative positions of the three marker beds used are illustrated in the spontaneous potential and deep resistivity logs of the five wells in Figure 1. There is good correlation among shale layers on all of the logs. The V12 marker occurs throughout the area above the B27 reservoir sand, the V5 marker is recognizable everywhere below the A22 sand, and the V2

marker can be recognized throughout the area above the A8 sand. Frio Formation sands are fluvial and comprise single, multiple, and amalgamated lenticular sand bodies.

Cross-sections were constructed through wells 151 and 145 to relate the P -wave sonic velocity with the lithology. For example, the cross-section given in Figure 2 includes the calculated lithology and the compressional-wave velocity between depths of 3750 ft (1143 m) and 3900 ft (1189 m). The V2 marker occurs immediately above the A8 sand reservoir. The lithology in well 145 shows an interval of 20 ft (6 m) of sand below the V2 marker, and well 151 shows an interval of about 15 ft (5 m) of sand.

Because shale markers can be correlated readily across the Stratton field, they can help define the relationship between structure and stratigraphy. Figure 3 shows the location of three wells and the contour map of geologic marker V2. The contours were plotted using information from about 40 wells from the Stratton field. The three wells in Figure 3 are the wells used to conduct the interwell logging experiments.

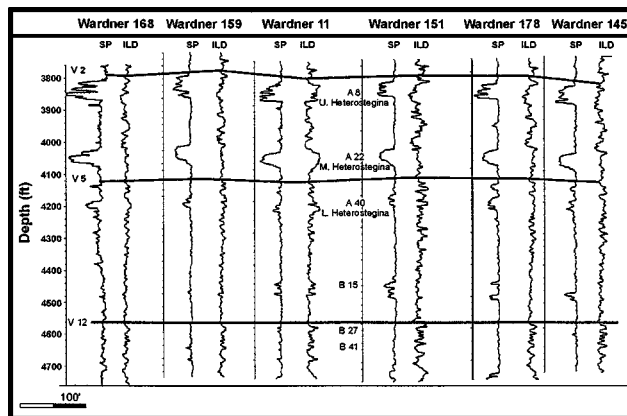


FIG. 1. Three markers appear on the logs as zones of low resistivity, each having uniquely distinguishable characteristics that can be identified on every well log. Examples of spontaneous potential (SP) and deep induction (ILD) logs are shown for six wells in the study area.

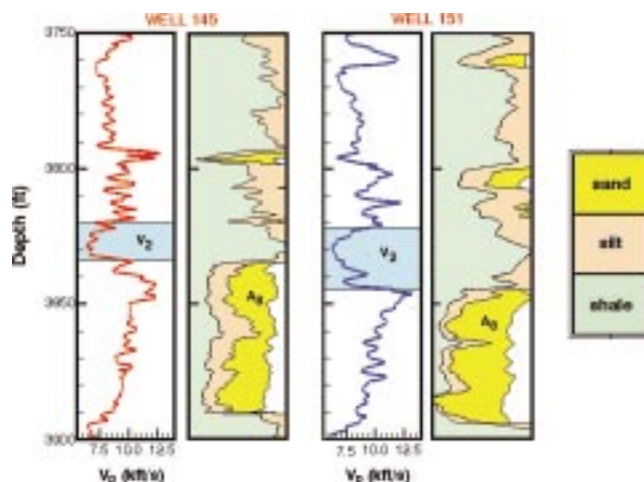


FIG. 2. Lithological columns for wells 151 and 145, showing the V2 shale marker and associated low-velocity zone.

Interwell seismic experiments were conducted between three wells at the Stratton field. The source well, 151, lies 1730 ft (527 m) from well 145 and 2744 ft (836 m) from well 159. The casing in well 145 was imperfectly bonded to the formation, so only hydrophone data were recorded there, while three-component data were recorded in well 159 using the Texaco three-component geophone system. The source used was Texaco's multiple air gun, a tool comprised of three air guns spaced 27 inches apart. Each gun has a 40-cubic-inch displacement, and all three are fired simultaneously with each shot. Tool size requirements mandated a minimum internal casing diameter of 4.89 inches in 5.5-inch casing. The three selected wells—145, 151, and 159—fulfilled the minimum casing size requirements for the experiments. Figure 4 shows a cross-section of the three wells as well as source and detector positions for the experiments.

To demonstrate the presence of guided waves in the interwell seismic data set, we focus on the analysis and interpretation of data associated with the V2 and V5 geologic shale markers. Structural maps of these units are given in Gorody and Parra (1999), which show that the V2 shale unit is more heterogeneous (thickness variability) than the V5 unit. Qualitatively similar results are obtained for the V12 and well 151–159 experiment. The data from this experiment have a poor S/N ratio and are somewhat more difficult to interpret.

Analysis of waveguide V2

The observed seismic data for the V2 zone are shown in Figure 5. The source was placed several feet above the

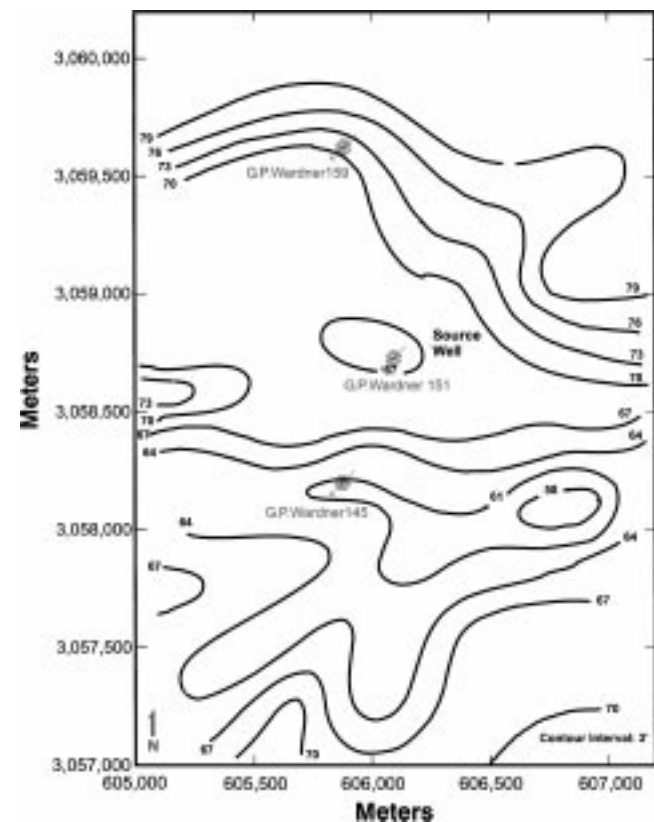


FIG. 3. Isopach map showing the estimated thickness of the V2 low-velocity shale.

predicted waveguide layer. Receivers were at 2-ft (0.6-m) spacings near the source depth and 10-ft (3-m) spacings away from the source depth, with a total coverage of about 200 ft (61 m) of wellbore. Tube waves are quite prominent in the recorded hydrophone data and obscure some of the recorded signal (Figure 5a). A tube-wave filter was applied to reduce wave amplitude (Figure 5b).

The primary signal arrives at roughly the average P -wave velocity. Most of the signal energy is 100–300 Hz, so the wavelengths vary from about 30 ft (9 m) to 80 ft (24 m). It is perhaps not surprising, then, that there is no strong variation in the character of the first arrival with depth over the measured interval. The leaky-mode guided wave arrives shortly after and is partially obscured by the direct wave.

Figure 6a shows the amplitude–depth distribution curves of the wavefield spectrum based on the receiver positions of the seismogram in Figure 5b. The window for leaky-mode analysis extends from 0.24 to 0.26 s. The signal arrives at 0.245 s after the initial strong arrival. A Fourier transform was taken

of each windowed seismogram, and the magnitude of the response for signal frequencies was plotted versus depth in the receiver well. Good confinement of energy was seen near the waveguide in the 150-Hz band. The measured amplitude had a minimum at the approximate waveguide center, suggesting an asymmetric leaky mode (Dresen and Ruter, 1994; Parra, 1996). To confirm the presence of the asymmetric mode observed in Figure 6a, we calculated a synthetic seismogram based on the actual sonic well log (Figure 6b) using a 1-ft resolution; as such, the seismogram incorporates a detailed model of the lithology formed by shales and sandstones. The synthetic seismograms were produced using a 2-D finite-difference viscoelastic computer program, assuming no lateral variations in lithology. A small amount of viscoelastic attenuation was

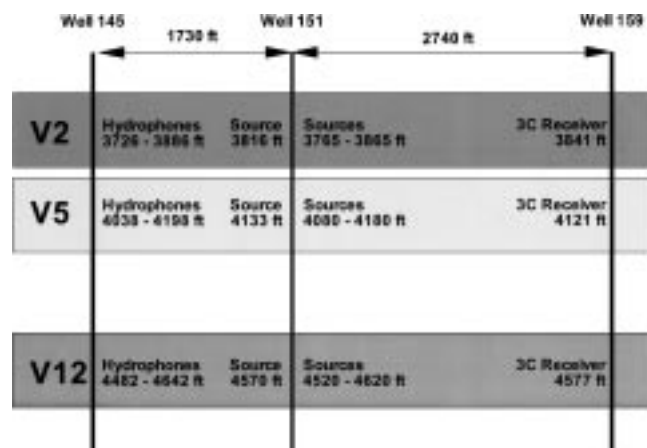


FIG. 4. Borehole geometry for the continuity logging experiments at the Stratton gas field.

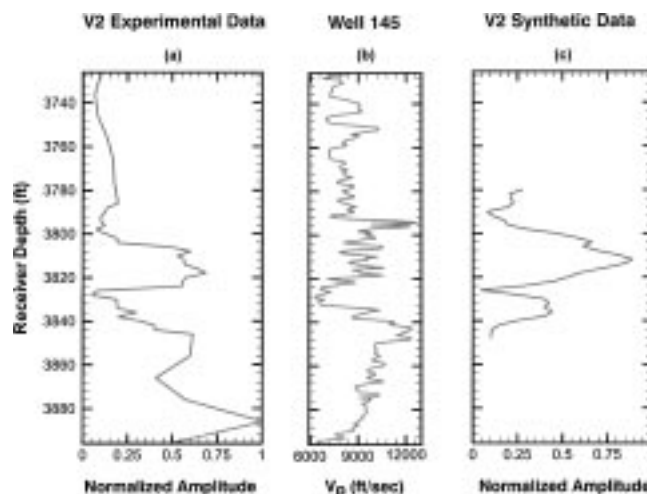


FIG. 6. (a) Amplitude–depth distribution of energy from the experimental seismogram of Figure 5a. An asymmetric leaky mode appears in the 150-Hz band. (b) P -velocity well log from well 145. The low-velocity shale layer is clearly visible. (c) Amplitude–depth distribution of energy for a synthetic seismogram assuming full continuity of the low-velocity zone. The asymmetric mode is also visible here.

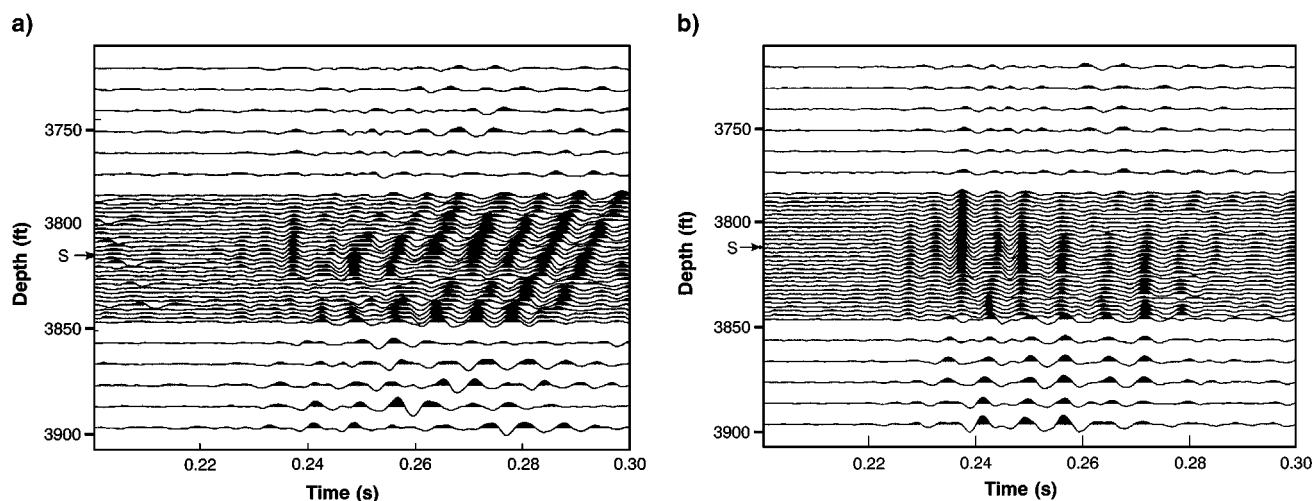


FIG. 5. Experimental common source seismogram with source at 3816 ft (1163 m) in well 151. Vertical axes show receiver depth in well 145. Receivers are closely spaced near the low-velocity zone. The well separation is 1730 ft (527 m). (a) Recorded data, including high-amplitude tube waves. (b) Data processed for tube-wave removal. The window for leaky-mode analysis extends from 0.24 to 0.26 s. An asymmetric mode is visible in this time window, centered on 3825 ft (1166 m).

introduced to damp out spurious reflections. The synthetic seismogram shares most of the features of the experimental data set, including confinement of energy at a depth of around 3830 ft (1167 m) and higher amplitude in the fast arrival at shallower depth. Thus, we determined the amplitude–depth distribution (Figure 6c) from the synthetic seismogram. The synthetic amplitude–depth distribution curve is given in the same plot with the observed distribution and the velocity well log. The figure shows agreement between observed and calculated distributions. The strong confined energy is associated with the region between 3810 ft (1161 m) and 3820 ft (1164 m), which corresponds to the region above the low-velocity region, V2.

The above correlation demonstrates the presence of trapped energy in the data. Although the synthetic data computed on the basis of a layered-earth model revealed the presence of higher frequency dispersive modes, we could not demonstrate that the observed guided modes are dispersive. One explanation of the lack of higher frequency modes is the thickness variation of shale marker V2, which varies an average of 7 ft (2 m) between wells 145 and 151 (see Figure 3). This thickness variation can produce loss of energy or scattering attenuation that can prevent the propagation of higher frequency modes at a well separation of 1730 ft (527 m). On the other hand, shale marker V5 exhibits little thickness variation, relative to V2, in the interwell region between wells 145 and 151 (Gorody and Parra, 1999).

Processing and analysis of seismic waves in waveguide V5

A cross-section was constructed through wells 151 and 145 to relate the *P*-wave sonic velocity with the lithology in the region of waveguide V5. The cross-section given in Figure 7 includes the calculated lithology and the compressional-wave velocity between depths of 4050 ft (1234 m) and 4200 ft (1280 m). The V5 marker occurs immediately below the A22 sand reservoir. In this case, a connected marker can be used to resolve the origin of the A22 sands.

The air gun source was placed at a depth of 4133 ft (1260 m), just above waveguide V5. Hydrophone data were recorded in

well 145 at 2-ft (0.6-m) intervals from depths of 4098 ft (1249 m) to 4158 ft (1267 m) and at 10-ft (3-m) intervals for an additional 50 ft (15 m) beyond these depths. The hydrophone data were filtered with a highpass filter of 90 Hz (Figure 8).

A discrete layered model was constructed for the waveguide zone. Leaky- and normal-mode dispersion curves were calculated using a layered model (Parra et al., 1998), and synthetic seismograms were produced using finite-difference modeling. The pressure seismogram is based on the actual logs to a 1-ft resolution. As such, the seismogram incorporates a more detailed model of the lithology than the computed dispersion curves.

Velocity frequency analysis was applied to the experimental and synthetic data to determine the dispersive character of the signal. The contour plots were determined from full waveforms using a short-term Fourier transform (Cohen, 1989). The selected traces are for source and detector positions at depths of 4133 ft (1260 m) and 4140 ft (1262 m). In Figures 9a and 9b, the computed dispersive modes are shown as heavy lines superimposed on the real and synthetic group velocity contours of leaky modes, respectively, for waveforms near the top of the waveguide boundary. The predicted dispersion curves are labeled 1, 2, and 3 in Figure 9. In this analysis, the group velocity curves (heavy lines) were computed using a combination of 2-D bracketing and minimization techniques (Parra and Xu, 1994). The dispersion contours determined by velocity–frequency analysis agree with theoretical group velocity curves. The first event is observed to be dispersive, varying from about 8000 ft/s (2438 m/s) to about 7000 ft/s (2134 m/s) over 100 to 400 Hz. Velocity therefore decreases with frequency within the 300-Hz frequency window. This is consistent with synthetic leaky-mode group velocity curves for the second and third modes. The fact that leaky modes in the observed data are characterized with computer models suggests that the V5 shale marker is connected and continuous between wells. A similar situation was observed in a data set recorded between wells separated by 100 m (330 m) at the Gypsy test site, Oklahoma.

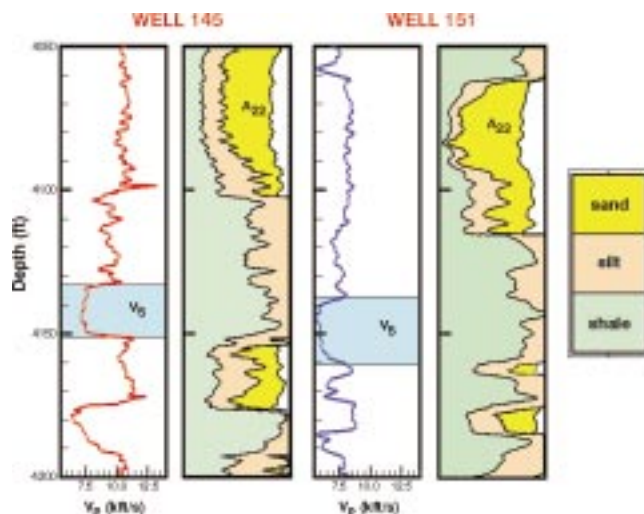


FIG. 7. Lithological columns for wells 151 and 145 showing the V5 shale marker and associated low-velocity zone.

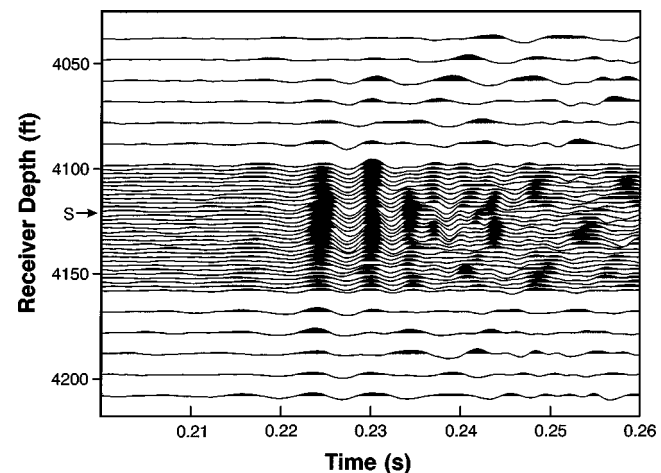


FIG. 8. Experimental common source seismogram with source at 4133 ft (1260 m) in well 151. Vertical axes show receiver depth in well 145. Receivers are closely spaced near the low-velocity zone. The well separation is 1730 ft (527 m). The window for leaky-mode analysis extends from 0.23 to 0.25 s. An asymmetric mode is visible in this time window, centered on 4140 ft (1262 m).

Because in this data set multioffset measurements were available, it was possible to demonstrate that the only way to excite leaky modes in a low-velocity zone was when source and detectors were within the waveguide or at near offsets of the waveguide boundaries (see Parra et al., 1998). This experiment showed that leaky modes can be excited in low-velocity zones; consequently, the presence of leaky modes in the data helps to interpret waveguide targets. In the Stratton gas field, we are demonstrating that guided waves can propagate at distances comparable to the separation of gas wells (i.e., 800 m, or 2624 ft).

A second method to identify guided waves in the data is using amplitude–depth distribution curves that can be obtained directly from the seismogram. We have produced amplitude–depth distribution curves from the observed and synthetic seismograms. These curves are shown together with the *P*-wave velocity log in Figure 10. A strong correlation is observed between the experimental and synthetic amplitude–depth distribution curve near the boundary of the V5 zone. This curve represents an asymmetric leaky mode in the 200-Hz frequency band. This correlation and the above dispersion analysis demonstrate that the V5 low-velocity zone is indeed continuous between wells 145 and 151. In particular, waveguide V5 is more continuous than waveguide V2.

In the following section we propose a more practical way to present the trapped energy in a waveguide.

IMAGES OF CONTINUOUS AND DISCONTINUOUS TARGETS

In crosswell traveltimes and attenuation tomography, as well as in reflection imaging, the results are presented as contours or images that can be associated with the subsurface geology or rock physical properties of interest. This helps reservoir engineers and earth scientists make more informed decisions in the course of their work. The standard processing method to produce images from multiple-offset seismic measurements (e.g., crosswell seismic tomography) between wells

is the back-projection method (Hardage, 1992). This type of method works well if large offsets are used. This may require a lot of data acquisition time in the wells. However, despite the operation time this can produce a good image of the subsurface. On the other hand, the continuity logging method based on guided waves does not need large offsets between source and receivers to excite guided waves in a low-velocity zone of interest. Trapped energy in the form of guided waves can be identified using modeling and signal analysis from the continuity data set. However, an image that can be understood by reservoir engineers may be difficult to produce from a data set that does not have large offsets. In fact, back projection does not provide an interpretable image from a practical continuity logging data set.

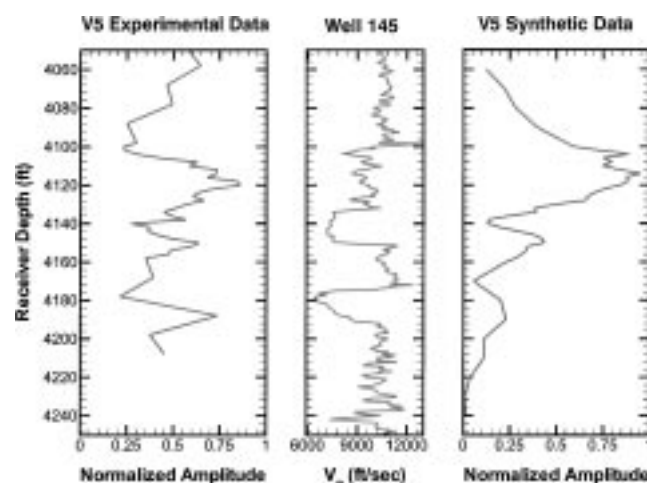


FIG. 10. (a) Amplitude–depth distribution of energy from the experimental seismogram of Figure 8. An asymmetric leaky mode appears in the 150-Hz band. (b) *P*-velocity well log from well 145. The low-velocity shale layer is clearly visible. (c) Amplitude–depth distribution of energy for a synthetic seismogram assuming full continuity of the low-velocity zone. The asymmetric mode is also visible here.

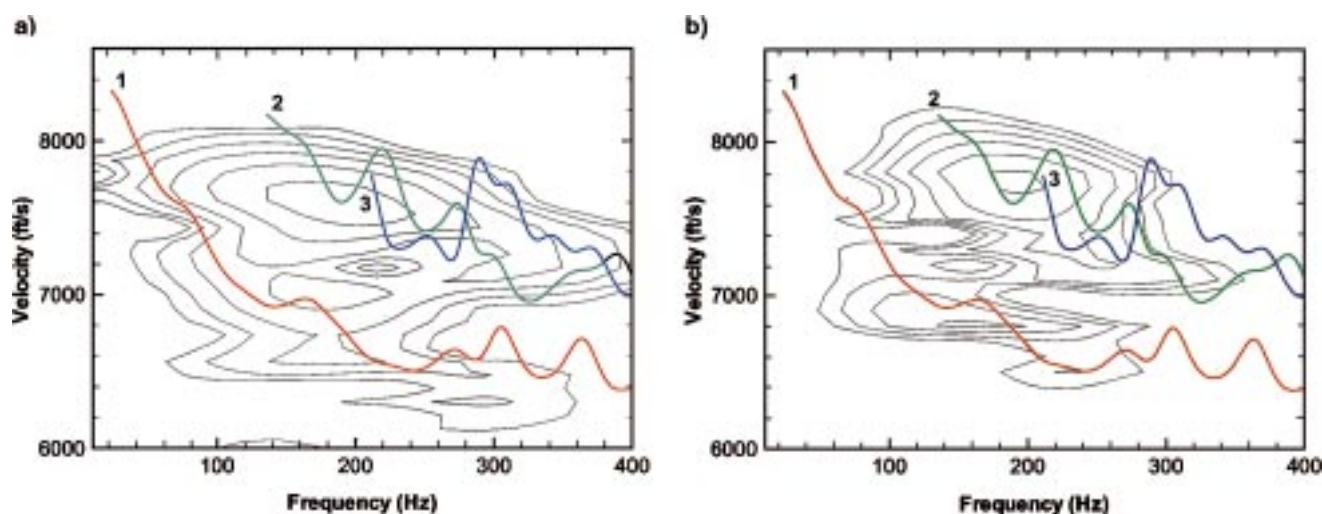


FIG. 9. (a) Velocity–frequency analysis of experimental data from Figure 8, showing dispersive behavior of the leaky modes. The predicted dispersion curves of the first three leaky modes are overlain and are labeled 1, 2, 3. (b) Velocity–frequency analysis of synthetic seismogram, assuming full continuity of the low-velocity zone. Again, the predicted dispersion curves of the first three leaky modes are overlain. The experimentally observed dispersion is quite similar to both that of the synthetic seismogram and the predicted mode dispersion.

To overcome this problem we had to compromise by choosing (1) an inaccurate back-projection image or (2) amplitude–depth distribution curves supported with dispersion analysis of guided modes. We decided on the second approach but added a new dimension to the final result. This required converting the full waveform recorded at each detector position into the frequency domain. As a result we can create an image for all detector positions for a given source position. If we have several source positions, we can produce several images that can be stacked together to produce the final image associated with that data set.

Before we applied the imaging technique to the Stratton data set, we illustrated the method using synthetic data associated with two simple geometries. For the real example, we chose the seismic data acquired in the interwell region of geologic marker V5.

An 11-source, 25-receiver crosswell data set was simulated using finite-difference modeling. The crosswell geometry was that of either a continuous or a faulted waveguide in an un-

bounded uniform medium. The waveguide was 15 ft (4.5 m) thick, and the fault throw (when present) was 45 ft (13.5 m). Although these are idealized cases, a realistic well separation of 1500 ft (457 m) and realistic crosswell frequencies of 100 to 400 Hz were used. A 5-ft spacing in sources and receivers yielded a source coverage of 50 ft (15 m) and receiver coverage of 120 ft (37 m). The medium was attenuating with a Q of 100 in all materials.

Figure 11 shows the response in the depth–frequency domain of an ideal continuous waveguide and an ideal fault waveguide. In the continuous waveguide, energy at all frequencies is centered on the waveguide. In the discontinuous case, the low-frequency part successfully converts to the upper waveguide after the fault, while the higher frequencies remain centered in the original waveguide level. The question is, can such effects be observed in real data? We expect that the guided waves observed in the real data will be coupled with other waves so the full-waveform signatures will be difficult to interpret with simple models such as the one shown in Figure 11. The

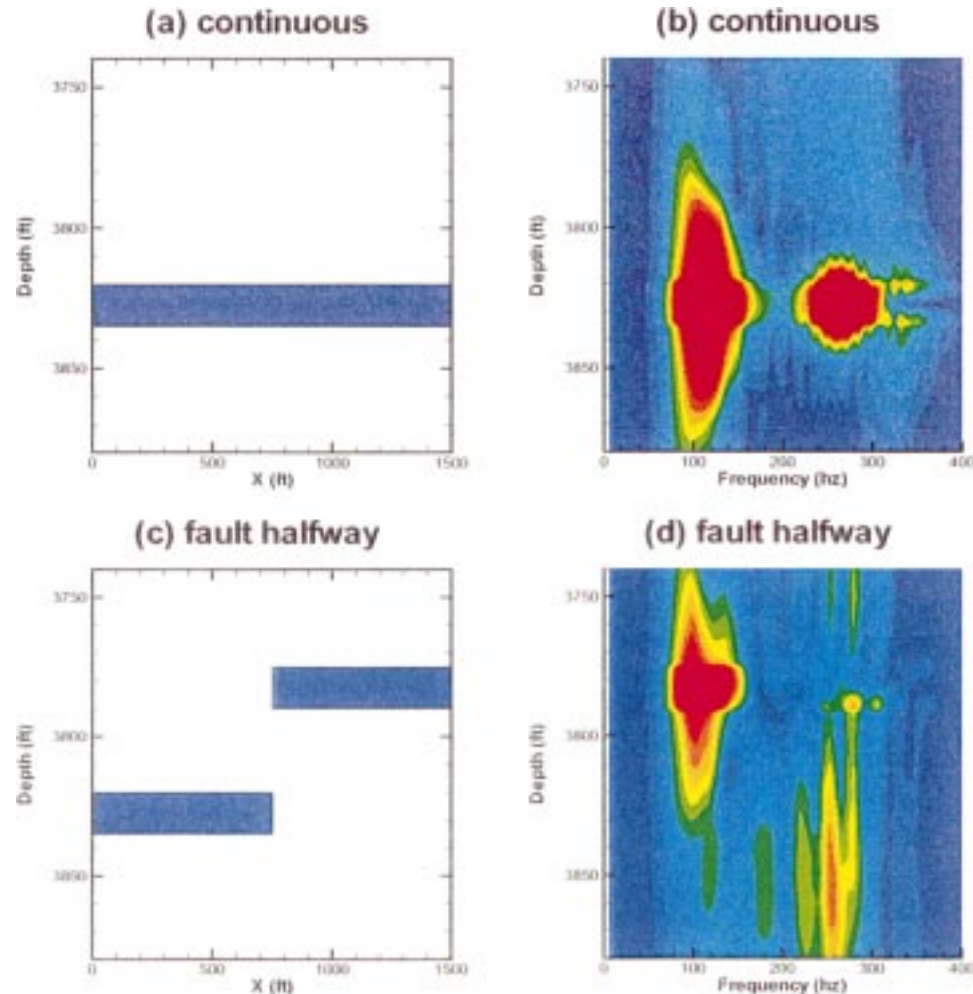


FIG. 11. (a) Geometry of an ideal continuous low-velocity waveguide. (b) Depth–frequency energy distribution based on common source seismogram, with the source in the waveguide on the left side. Depth indicated is receiver depth, with receivers on the right side. Symmetric modes appear near 100 and 260 Hz, while an asymmetric mode is visible near 340 Hz. (c) Geometry of an ideal faulted waveguide. (d) Depth–frequency energy distribution for a common source seismogram, with the source in the faulted waveguide on the left of (c). Depth indicated is the receiver depth on the right edge of (c). The lower-frequency leaky modes successfully transition from the deeper to the higher low-velocity zone, while the high-frequency modes do not make the transition.

interpretation will be complicated by multiple low-velocity zones (leading to multiple guided waves) and other reflectors near the waveguide, which will lead to a spurious high-frequency signal. Thus, to identify the presence of guided waves in a seismogram will require an understanding of the guided-wave signal characteristics based on multiple layered models as well as processing skills and a knowledge of the site geology.

Figure 12 shows the V5 geologic marker. This provides a good example of the kinds of signatures we expect to see, but in this particular example the two highest energy peaks (4050 and 4120 ft) (1234 m and 1256 m) are not aligned with low-velocity zones. This is not a sign of discontinuity because none of the energy in these two areas is aligned with the waveguide. These are probably reflections from the layered media. Energy in the waveguide at 4135 to 4150 ft (1260 to 1265 m) is associated with asymmetric modes. Specifically, the mode at 150 Hz and a 4140-ft depth that appears weaker is partially obscured by the amplitude high near 4120 ft. In addition, a second symmetric mode appears to have been excited in the waveguide at 4180 ft. The horizontal character of the energy at 4190 ft (1277 m) implies waveguide continuity. Since we are dealing with a real geological situation in which waveguides without perfectly horizontal boundaries are immersed in a multilayered 3-D structure, we do not expect to have perfect asymmetric and asymmetric modes such as those shown in Figure 11. However, if more source locations had been available at these depths, we might have been able to obtain a better picture of wave behavior and have a clearer idea of formation continuity.

CONCLUSIONS

The predicted and measured velocity dispersions of the first arrival near the waveguide are consistent, indicating that the measured pulse consists substantially of leaky modes. This in turn indicates a high degree of continuity in shale markers.

In addition, modeling shows that asymmetric modes tend to be excited more strongly with the source outside the waveguide. Normal modes predicted in the synthetic data are not observed. This may be because they are obscured by high-amplitude tube waves or because of higher-than-predicted attenuation of the normal modes. The results of the processing and modeling illustrate that continuity logging can be used in hydrocarbon reservoir characterization to predict the continuity of thin, low-velocity shale markers between gas wells. In addition, continuity logging allows us to confirm that low-velocity shale markers are truly continuous stratigraphic markers. The tests performed at Stratton field show that each of three low-velocity zones can be identified on all of the well logs and that the zones are continuous between wells 145 and 151.

In addition, the images of the waveguides can be improved if more source fans are acquired. Specifically, the V5 geological marker image was constructed using only one source position and several detector positions. Such images can help the geologist and reservoir geophysicist predict the degree of continuity or discontinuity of the geological units of interest between wells. Results of this study illustrate that continuity logging can be applied to evaluate the continuity of thin, low-velocity shale markers between gas wells. Because we were able to establish the continuity of thin shales across the study area, we are confident that no small faults are occurring below the limits of surface seismic resolution that offset sands and potential production. Because many low-velocity zones in the Frio Formation are likely to be shale bodies, high-resolution continuity logging can help predict the presence of flow barriers. This is important in enhanced oil recovery applications such as waterflooding, carbon dioxide flooding, and steamflooding, where traveltimes tomography is particularly useful. Accordingly, continuity logging can profitably extend the market niche for traveltimes tomography.

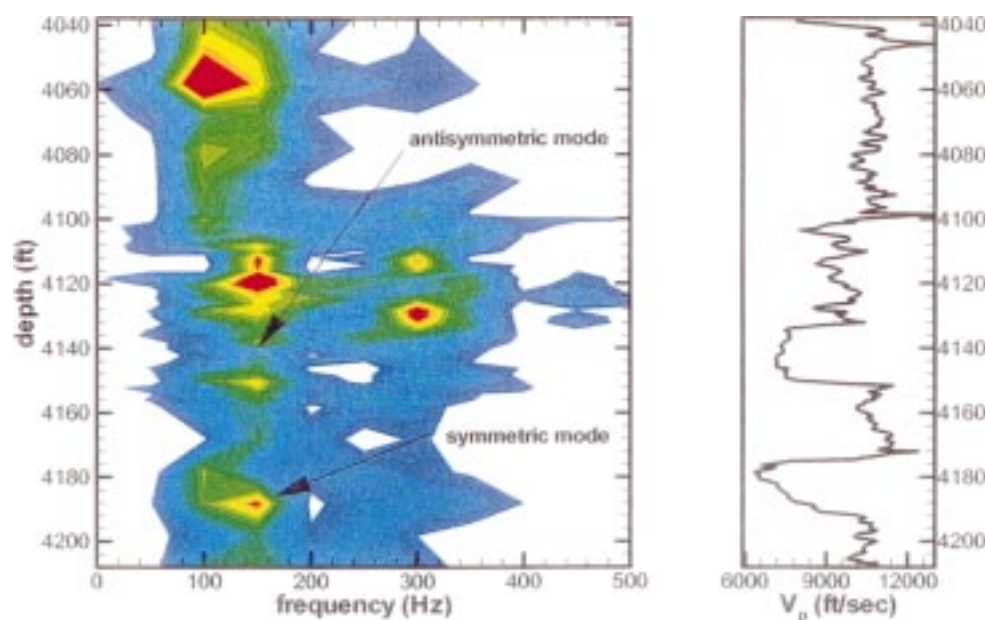


FIG. 12. Experimentally observed depth-frequency energy distribution for the V5 waveguide zone. The asymmetric mode at 150 Hz and 4140 ft (1262 m) depth is partially obscured by the amplitude high near 4120 ft (1256 m). Another symmetric mode appears to have been excited in the low-velocity layer at 4180 ft (1274 m). These effects are also reproduced in the synthetic seismograms (see Figure 10).

ACKNOWLEDGMENTS

This work was supported by the Gas Research Institute, contract 5093-260-2600. The assistance of R. Parker and permission granted by GRI to publish this paper are acknowledged. We wish to thank Texaco E&P Company for providing in-kind participation. In particular we thank D. Melton and D. Howlett. We also thank Union Pacific Resources Company for its contribution to the data and access to the Stratton field site. The comments and suggestions of *Geophysics* reviewers are appreciated.

REFERENCES

- Aki, K., and Richards, P. G., 1980, Quantitative seismology: Theory and methods, I: W. H. Freeman & Co.
- Apsel, R. J., 1979, Dynamic Green's function for layered media and applications to boundary value problem: Ph.D. thesis, Univ. of California at San Diego, La Jolla.
- Buchanan, D. J., 1983, In-seam seismology: A method for detecting faults in coal seams, in Fitch, A. A., Ed., Developments in geophysical exploration methods, 5: Applied Science Publ. Ltd., 1-34.
- Cohen, 1989, Time-frequency distributions—A review: IEEE Proceedings, 77, 941-981.
- Dresen, L., and Ruter, H., 1994, Seismic coal exploration part B: In-seam seismic: Pergamon Press, Inc.
- Dunkin, J. W., 1965, Computation of modal solutions in layered elastic media at high frequencies: Bull. Seis. Soc. Am., 55, 156-160.
- Gorody, A. W., and Parra, J. O., 1999, Continuity logging for mapping low velocity geological markers: Gas Tips, 5, 4-10.
- Hardage, D. A., 1992, Crosswell seismology and reverse VSP: Geophysical Press.
- Kundu, T., and Mal, A. K., 1985, Elastic waves in a multilayered solid due to a dislocation source: Wave Motion, 7, 459-471.
- Kennett, B. L. N., and Kerry, N. J., 1979, Seismic waves in a stratified half space: Geophys. J. Roy. Astr. Soc., 57, 557-583.
- Kosters, E. C., Bebout, D. G., Seni, S. J., Garrett, C. M., Jr., Brown, L. F., Hamlin, H. S., Dutton, S. P., Ruppel, S. C., Finley, R. J., and Tyler, N., 1989, Atlas of major Texas gas reservoirs: Univ. of Texas at Austin Bureau of Economic Geology.
- Kupradze, V. D., 1979, The three-dimensional problems of the mathematical theory of elasticity and thermoelasticity: North Holland Publ. Co.
- Laster, S. J., Goreman, J. A., and Linville, A., 1965, Theoretical investigation of modal seismograms for a layer over a half space: Geophysics, 30, 571-596.
- Levey, R. A., Finley, R. J., and Sippel, M. A., 1994, Quantifying secondary gas resources in fluvial/deltaic reservoirs: A case history from Stratton field, south Texas: Univ. of Texas at Austin Bureau of Economic Geology, R.I. 221.
- Mal, A. K., 1988, Guided waves in layered solids with interfacial zone: Internat. J. Eng. Sci., 26, 873-881.
- Parra, J. O., 1996, Guided seismic waves in layered poroviscoelastic media for continuity logging applications: Model studies: Geophys. Prosp., 55, 403-425.
- Parra, J. O., and Xu, P.-C., 1994, Dispersion and attenuation of acoustic guided waves in layered fluid-filled porous media: J. Acoust. Soc. Am., 95, 91-98.
- Parra, J. O., Sturdivant, V. R., and Xu, P.-C., 1993, Interwell seismic transmission and reflection through a dipping low-velocity layer: J. Acoust. Soc. Am., 93, 1954-1969.
- Parra, J. O., Zook, B. J., P.-C., Xu, and Brown, R. L., 1998, Transmission and detection of guided seismic waves in attenuating media: Geophysics, 63, 1190-1199.
- Rader, D., Schott, W., Dresen, L., and Ruter, H., 1985, Calculation of dispersion curves and amplitude-depth distribution of Love channel waves in horizontally layered media: Geophys. Prosp., 33, 800-816.
- Schmidt, H., and Tango, G., 1986, Efficient global matrix approach to the computation of synthetic seismograms: Geophys. J. Roy. Astr. Soc., 84, 331-359.

APPENDIX A

WAVE PROPAGATION IN A STRATIFIED TRANSVERSELY ISOTROPIC MEDIUM

Formulation

To develop the general solution of a point force in a layered transversely isotropic (TI) medium, we express the displacement-stress matrix in terms of upgoing and downgoing waves of unknown wave coefficients η_j . Each layer is characterized by five elastic constants c_{11} , c_{12} , c_{13} , c_{33} , and c_{44} and the density ρ . The displacement-stress matrix in the wavenumber domain for the j th layer of the TI medium is given by

$$\mathbf{u}_j = \mathbf{J}_j \mathbf{e}_j \eta_j, \quad (\text{A-1})$$

and

$$\mathbf{e}_j = \text{diag}(\exp(-v_j z^-), \exp(-\chi_j z^-), \exp(v_j z^+), \exp(\chi_j z^+)),$$

in which

$$z^- = z - z_{j-1} \quad \text{and} \quad z^+ = z - z_j.$$

The matrix \mathbf{J}_j is written as

$$\begin{bmatrix} -k v_j & k \chi_j & -k v_j & k \chi_j \\ -\gamma_j^2 f_j & \Omega_j^2 f_j & \gamma_j^2 f_j & -\Omega_j^2 f_j \\ -c_{44}^{(j)} k [v_j^2 - \gamma_j^2 f_j] & c_{44}^{(j)} k [\chi_j^2 - \Omega_j^2 f_j] & c_{44}^{(j)} k [v_j^2 - \gamma_j^2 f_j] & -c_{44}^{(j)} k [\chi_j^2 - \Omega_j^2 f_j] \\ -[c_{13}^{(j)} k^2 + c_{33}^{(j)} \gamma_j^2 f_j] v_j & [c_{13}^{(j)} k^2 + c_{33}^{(j)} \Omega_j^2 f_j] \chi_j & [-c_{13}^{(j)} k^2 + c_{33}^{(j)} \gamma_j^2 f_j] v_j & [c_{13}^{(j)} k^2 + c_{33}^{(j)} \Omega_j^2 f_j] \chi_j \end{bmatrix}, \quad (\text{A-2})$$

where

$$\mathbf{u}_j = [u_1^{(j)}, u_2^{(j)}, \sigma_{21}^{(j)}, \sigma_{22}^{(j)}]^T,$$

$$\eta_j = [\eta_1^{(j)}, \eta_2^{(j)}, \eta_3^{(j)}, \eta_4^{(j)}]^T,$$

where

$$\gamma_j^2 = v_j^2 - \beta_j^2,$$

$$\Omega_j^2 = \chi_j^2 - \beta_j^2,$$

$$f_j = \frac{c_{44}^{(j)}}{c_{13}^{(j)} + c_{44}^{(j)}},$$

and

$$\beta_j^2 = \left[\frac{c_{11}^{(j)}}{c_{44}^{(j)}} k^2 - \frac{\omega^2 \rho_j}{c_{44}^{(j)}} \right].$$

The wavenumbers χ_j and v_j in equation (A-2) are derived from the Green's function in the wavenumber domain of a point force in a TI unbounded medium, which is given by Kupradze (1979). Thus, these wavenumbers are obtained from the relationship

$$\begin{aligned} \begin{pmatrix} \chi_j^2 \\ v_j^2 \end{pmatrix} &= \frac{S_j}{4c_{44}^{(j)}c_{33}^{(j)}} \left[\left(k^2 - \frac{\omega^2 \rho_j}{S_a^{(j)}} \right) + \left(k^2 - \frac{\omega^2 \rho_j}{S_b^{(j)}} \right) \right] \\ &\pm \frac{1}{2} \left\{ \frac{S_j^2}{4c_{44}^{2(j)}c_{33}^{2(j)}} \left[\left(k^2 - \frac{\omega^2 \rho_j}{S_a^{(j)}} \right) + \left(k^2 - \frac{\omega^2 \rho_j}{S_b^{(j)}} \right) \right]^2 \right. \\ &\quad \left. - \frac{4c_{11}^{(j)}}{c_{33}^{(j)}} \left(k^2 - \frac{\omega^2 \rho_j}{c_{11}^{(j)}} \right) \left(k^2 - \frac{\omega^2 \rho_j}{c_{44}^{(j)}} \right) \right\}^{1/2}, \quad (\text{A-3}) \end{aligned}$$

in which

$$S_a^{(j)} = \frac{S_j}{2c_{33}^{(j)}},$$

$$S_b^{(j)} = \frac{S_j}{2c_{44}^{(j)}},$$

and

$$S_j = c_{33}^{(j)}c_{11}^{(j)} + c_{44}^{2(j)} - (c_{13}^{(j)} + c_{44}^{(j)})(c_{13}^{(j)} + c_{44}^{(j)}).$$

As a check on the derivation given by equation (A-2), the corresponding solution for a layered isotropic medium is deduced. This is accomplished by replacing in equation (A-2) the TI parameters by those isotropic properties, i.e.,

$$c_{13}^{(j)} = \lambda_j$$

$$c_{11}^{(j)} = c_{33}^{(j)} = \lambda_j + 2\mu_j$$

and

$$c_{44}^{(j)} = c_{66}^{(j)} = \mu_j,$$

yields the displacement–stress matrix in the wavenumber domain. For this case, the matrix \mathbf{J}_j becomes

$$\mathbf{J}_j = \begin{pmatrix} -k & \chi_j & -k & \chi_j \\ -v_j & k & v_j & -k \\ 2\mu_j k v_j & -\mu_j(2k^2 - k_{sj}^2) & -2\mu_j k v_j & \mu_j(2k^2 - k_{sj}^2) \\ \mu_j(2k^2 - k_{sj}^2) & -2\mu_j k \chi_j & \mu_j(2k^2 - k_{sj}^2) & -2\mu_j k \chi_j \end{pmatrix}, \quad (\text{A-4})$$

where

$$k_{sj}^2 = \omega^2 \rho_j / \mu_j, \quad v_j = (k^2 - \omega^2 \rho_j / (\lambda_j + 2\mu_j))^{1/2},$$

and

$$\chi_j = (k^2 - k_{sj}^2)^{1/2}.$$

The coefficients of the stress–displacement matrix given by equation (A-4) are the same as those coefficients associated with the Green's function for an elastic isotropic medium derived by Apsel (1979).

Boundary conditions

The analysis of wave propagation in anisotropic layered media is a boundary value problem in which the motion is governed by the elastic-wave equation in each layer. In addition, the displacement and stress fields must satisfy (a) the conditions of continuity of displacements and tractions across each interface and (b) the radiation conditions above the layered medium $z \leq 0$ and in the underlying half-space $z \geq 0$. To avoid precision problems caused by the growing exponential in the individual matrices for large wavenumbers, the global matrix method (Schmidt and Tango, 1986; Mal, 1988) is implemented as an alternative to the traditional propagation approach to calculate the vector wave displacement and the pressure. To facilitate the global matrix analysis, equation (A-1) is written in its vector and matrix form,

$$\mathbf{u}_m(\mathbf{z}) = \mathbf{J}_m \mathbf{e}_m(\mathbf{z}) \boldsymbol{\eta}_m. \quad (\text{A-5})$$

In equation (A-5) the vector $[\boldsymbol{\eta}_m]$ contains the unknown wave coefficients of wave propagation in the positive and negative z -directions.

In the global matrix formulation, the boundary conditions at the layer interface are satisfied in the form of difference of field quantities across the layer interface. These conditions can be represented by using equation (A-5) as follows:

$$\begin{aligned} \mathbf{J}_{m+1} \mathbf{e}_{m+1}(\mathbf{z}_m) \boldsymbol{\eta}_{m+1} - \mathbf{J}_m \mathbf{e}_m(\mathbf{z}_m) \boldsymbol{\eta}_m \\ = \mathbf{u}_{m+1}(\mathbf{z}_m) - \mathbf{u}_m(\mathbf{z}_m), \end{aligned} \quad (\text{A-6})$$

where z_m is the coordinate of the interface between m th and $(m+1)$ th layers. For example, the radiation condition associated with the upper half-space is enforced to equation (A-6) for $m=1$ by making the downgoing part of $\{\boldsymbol{\eta}_1\}=0$. In a similar manner the radiation condition is applied to the lower half-space by making the upgoing part of $\{\boldsymbol{\eta}_{N+1}\}$ vanish.

An assembly of equation (A-6) for $m=2, 3, \dots, N$, each consisting of four rows, and the above-mentioned reduced

version of equation (A-6) for $m=1, N+1$, each containing two rows, forms a linear system of equations given by

$$\mathbf{G} \boldsymbol{\eta} = \mathbf{b}. \quad (\text{A-7})$$

In equation (A-7), the global matrix \mathbf{G} is composed of submatrices obtained from $\mathbf{J}_m, \mathbf{e}_m(\mathbf{z}_m)$, and $\mathbf{e}_{m+1}(\mathbf{z}_m)$ for $m = 1, 2, \dots, N + 1$. These submatrices contain coefficients associated with the physical properties of the anisotropic layered medium as well as the coordinates of the interfaces. The global

vector \mathbf{b} represents the external excitations (e.g., point forces or pressure sources) in the form of jump conditions at the interfaces z_m , $m = 1, 2, \dots, N + 1$, which are obtained from the right-hand side of equation (A-6). The wavenumber representation for a point source is given in Parra et al. (1993).